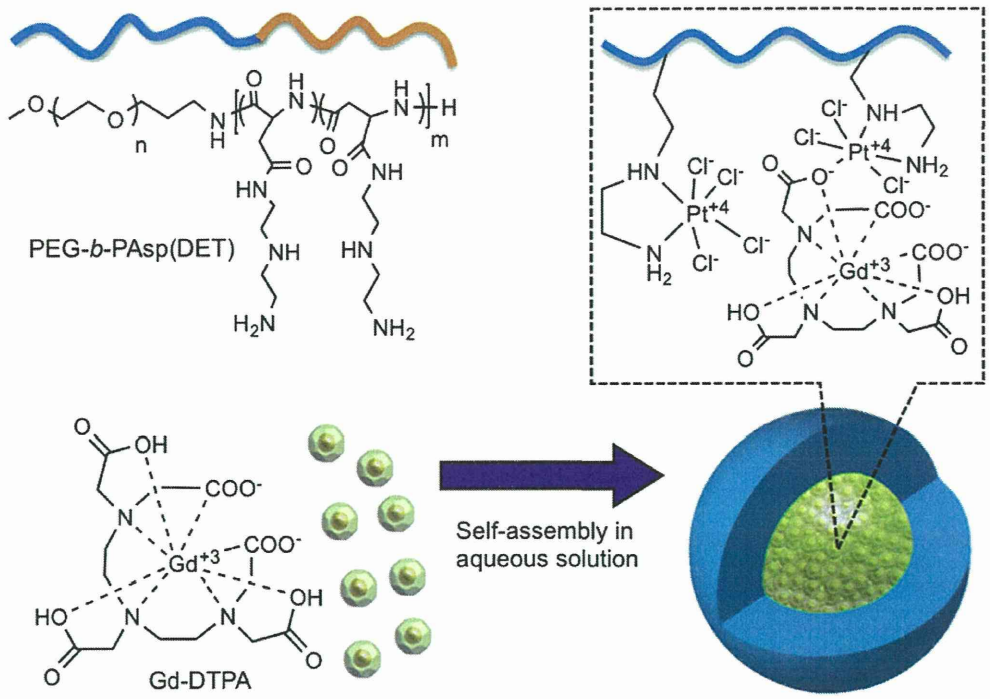

Scheme 1. Scheme illustration of the Gd-DTPA loaded micelle formation via polymer–metal complex formation.

incubated in 98 mL buffer of physiologic conditions (buffer: 10 mM PBS with 150 mM NaCl, temperature at 37 °C). 0.1 mL solution outside of the dialysis bag was sampled at defined time, and then the concentration of Gd-DTPA was measured by ICP-MS.

2.7. Characterization of r_1 relaxivity

The proton longitudinal relaxivity r_1, which is a parameter to evaluate the ability of contrast agents for MRI, can be determined from the change of the relaxation rate

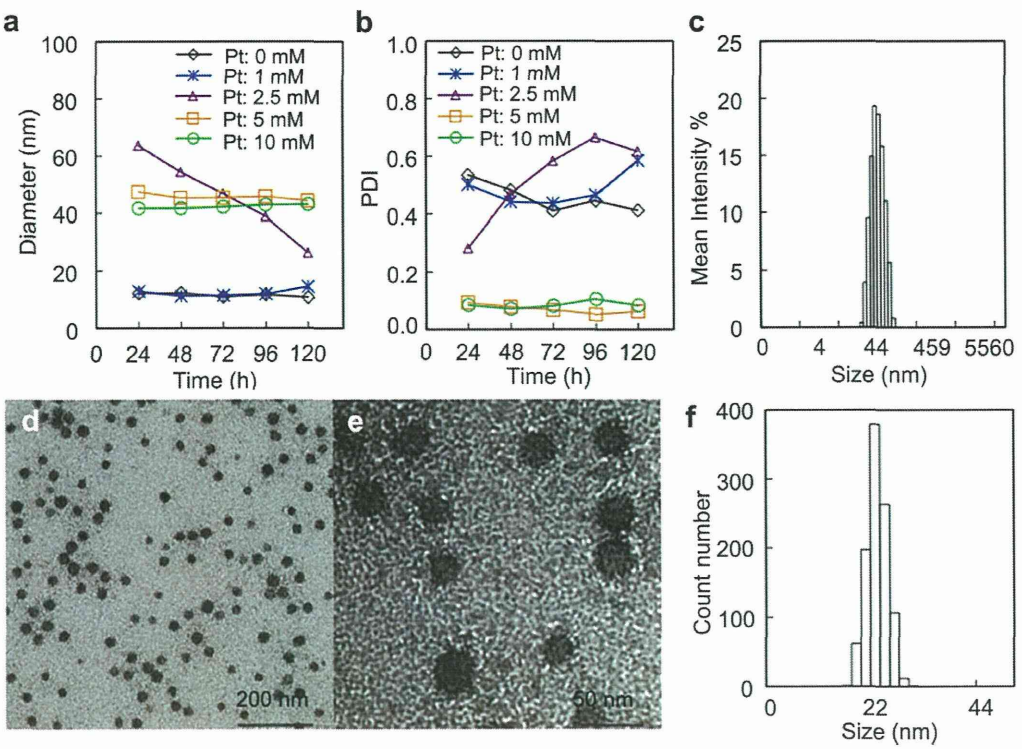

Fig. 1. Change in (a) average diameter and (b) polydispersity index (PDI) of Gd-DTPA/m with different Pt/Gd molar ratios, Gd-DTPA concentration was fixed at 5 mM, and Pt concentration ranged from 0 mM to 10 mM. (c) Size distribution measured by DLS. (d) and (e) TEM of Gd-DTPA/m. (f) Size distribution by number from TEM ($n = 1012$) calculated from Figure S6.

Table 1
Loading of Gd-DTPA/m prepared with different Pt/Gd ratio.

Sample (Pt:Gd-DTPA)	Pt linker loading	Gd-DTPA loading
0:5	0%	0%
1:5	~7.2%	~1.3%
2.5:5	~12.6%	~3%
5:5	~35%	~16%
10:5	~41%	~12%

Polymer PEG-*b*-PAsp (DET) 12k-45DP was used, the loading was calculated by dividing the drug amount to the total amount.

$1/T_1$ (s^{-1}) of water protons per mM concentration of CAs and calculated using expression $r_1 = (1/T_1 - 1/T_{1d})/[Gd]$, where $1/T_1$ is the longitudinal relaxation rate contrast in the presence of a paramagnetic species, $1/T_{1d}$ is the longitudinal relaxation rate contrast in the absence of a paramagnetic species and [Gd] is the concentration of paramagnetic CAs (mM). The T_1 values of Gd-DTPA, Gd-DTPA/m, or Gd-DTPA/K_2PtCl_6 solution of different Gd-DTPA/Pt ratios were measured at 37 °C in water or PBS buffer with a 0.59 T ^1H NMR analyzer (JNM-MU25A, JEOL) with a standard inversion-recovery pulse sequence.

2.8. Kinetic stability of Gd-DTPA/m

The stability of Gd-DTPA/m micelles under physiologic conditions was determined by DLS and static light scattering using Zetasizer Nano ZS90 (Malvern Instruments Ltd., UK). Changes of scattering light intensity were measured at defined time periods. A decrease in the scattering light intensity was associated with a decrease in the apparent molecular weight of the micelles and drug density inside the micelle core as well as in the micelle concentration. The size distribution and diameter of the Gd-DTPA/m were simultaneously monitored. The zeta-potential of Gd-DTPA/m was measured in phosphate buffer (10 mM) at pH 7.4 using Zetasizer Nano ZS90.

2.9. In vitro cytotoxicity evaluation

The cytotoxicity of Gd-DTPA/m against HUVEC and B16-F10 cell lines were evaluated by the CCK-8 assay. HUVEC and B16-F10 cells (5000 cells) were cultured with EGM-2 bullet kit and DMEM (containing 10% FBS), and then placed in 96-well plates, respectively. The cells were then exposed to Gd-DTPA, PEG-*b*-PAsp(DET), K_2PtCl_6 and Gd-DTPA/m for 72 h under 5% CO_2 at 37 °C. The Kit-8 solution was added, and followed by incubation under 5% CO_2 at 37 °C for 2.5 h. The absorbance at 450 nm of the produced WST-8 formazan in each well was measured using a using a micro-plate reader (Model 680, Bio-rad).

2.10. Cancer models

CDF_1 mice (female, 6 weeks old) were inoculated subcutaneously with C-26 cells (1×10^6 cells/mL). *In vivo* biodistribution, elemental mapping and MRI studies were performed when tumors were approximately 50 mm^3 in volume.

2.11. Biodistribution of Gd-DTPA/m

Gd-DTPA or Gd-DTPA/m was intravenously injected to the C-26 bearing mice at a dose of 78 μg/mouse on a Gd-DTPA basis. The mice were sacrificed after defined time periods (1, 4, 8 and 24 h). Tumors, livers, kidneys and spleens were excised. Blood was collected from the inferior vena cava, heparinized and centrifuged to obtain the upper plasma. Tissue samples were washed in PBS and weighed after removing excess fluid. The samples were dissolved in 90% HNO_3 and evaporated to dryness. The Pt and Gd concentrations were then measured by ICP-MS after the dried samples were dissolved in 1% HNO_3. The area under the curve (AUC) of a plot of liver, kidney, tumor and spleen drug concentration versus time was measured based on the trapezoidal rule up to 24 h after administration. Then, AUC ratios of tumor to liver, kidney and spleen are calculated.

2.12. Histology study

Mice bearing C-26 tumors were intravenously injected with Gd-DTPA/m at 100 μg/mouse on a Gd-DTPA basis. Twenty-four hours later, tumors were collected and immediately frozen in an acetone/dry ice mixture. The frozen samples were further sectioned at 6-μm thickness in a cryostat. Then, these thin sections were placed on glass slides, dehydrated in xylene and dehydrated with graded alcohols. These slides were stained with hematoxylin and eosin (H&E) and then samples were observed by using an AX80 microscope (Olympus, Japan).

2.13. In vivo MRI of Gd-DTPA/m

Solutions containing 0.2, 0.3, 0.4 and 0.5 mM Gd-DTPA or Gd-DTPA/m were placed in thin-wall PCR tubes, and then closed with flat caps for MR imaging at 1 T (Aspect, Aspect Imaging) and 7 T (BioSpec 70/20USR, Bruker). *In vivo* MR images were obtained using 1 T imaging spectrometer. For the T_1-weighted images of the mice, the following parameters were adopted: spin-echo method, repetition time (TR) = 400 ms, echo time (TE) = 11 ms, field of view (FOV) = 48 × 48 mm, matrix size = 256 × 256, and slice thickness = 2 mm. MR images were obtained from C-26 tumor bearing mice when the mean tumor volume was 100 mm^3. For all of the mice, transaxial T_1-weighted images were taken before injecting Gd-DTPA/m or Gd-DTPA as a control imaging. The mice were anesthetized with 1.8% isoflurane during the MRI experiments. The mice were injected i.v. with 0.22 mmol/kg of Gd-DTPA alone or 0.02 mmol/kg of Gd-DTPA/m based on Gd-DTPA. The transaxial T1W images were taken with a phantom containing water as a reference signal in defined time. The images were reconstructed and analyzed using ParaVision (Bruker Biospin) and Image J (NIH).

2.14. Element analysis using μ-SR-XRF

Micro-synchrotron radiation-induced X-ray fluorescence spectrometry imaging (μ-SR-XRF) was used to determine Gd-DTPA as well as Fe, Pt distribution in sections of solid tumor. Briefly, CDF_1 mice bearing C-26 tumor were intravenously injected with Gd-DTPA/m at 100 μg/mouse on a Gd-DTPA basis. Twenty-four hours later, tumors were collected and immediately frozen in acetone/dry ice, and then sliced using a cryostat and fixed on polypropylene sheets. μ-SR-XRF was performed using

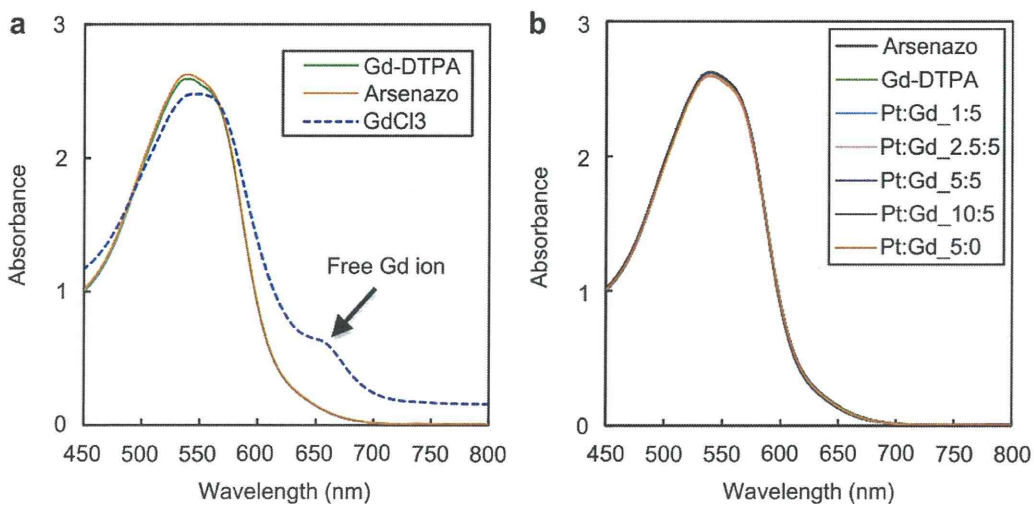

Fig. 2. Absorption spectrum of Arsenazo(III) solution with different mole ratios of Gd-DTPA and K_2PtCl_6 mixture solutions, the concentration of Gd-DTPA was maintained at 5 mM, the Pt concentration increased from 0 to 10 mM. The mixture of K_2PtCl_6 with Gd-DTPA did not compromise the stability of Gd-DTPA chelate.

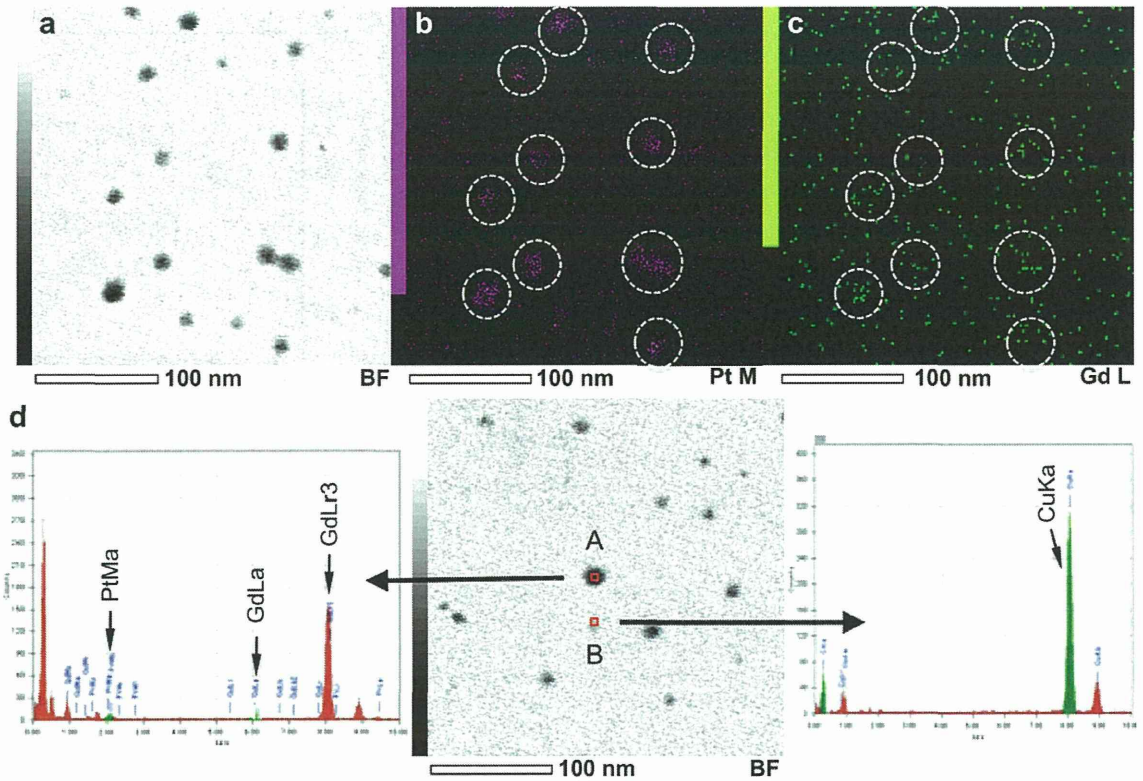

Fig. 3. EDS analysis of Gd-DTPA/m. (a) STEM image of Gd-DTPA/m. (b) Pt distribution under the STEM pattern. (c) Gd distribution under the STEM pattern. (d) EDX spectra of Gd-DTPA/m and background.

beam line 37XU at SPring-8 (Hyogo, Japan), operated at 8 GeV and ~100 mA. A photon beam with 14 keV of energy, a beam spot size of 1.3 × 1.3 μm^2, and an intensity of 1×10^{12} photons/s was used to irradiate the tissue sample. The fluorescence X-rays were measured using a Si-SSD in air at room temperature. Each sample on the acryl board was mounted on an x–y translation stage. The fluorescence X-ray intensity was normalized by the incident X-ray intensity, I_0, to produce a two-dimensional elemental map. An area of 250 × 250 μm^2 of the tissue sections was roughly scanned before μ-SR-XRF imaging.

3. Results and discussion

PEG-*b*-PAsp(DET) copolymers with different degree of polymerization (DP) (DP = 25, 35 and 45) were synthesized by aminolysis reaction of PEG-*b*-PBLA with diethylenetriamine (Scheme S1). PEG can hinder the interaction of the micelles with plasma proteins and prolong their circulation time in blood, while PAsp(DET) segments are minimally toxic and biodegradable as PAsp main-chain is fragmented from the nucleophilic attack of DET side chain via the formation of a succinimide ring [32]. Pt(IV) could form very stable chelates with amino groups of ethylenediamine and labile complexes with carboxylic groups [19,33]. Thus, as K_2PtCl_6 were mixed with PEG-*b*-PAsp(DET) and Gd-DTPA in aqueous solution, the block copolymers self-assembled into core–shell polymeric micelles carrying Gd-DTPA in the core as shown in Scheme 1. The K_2PtCl_6 concentration was found to be critical for the

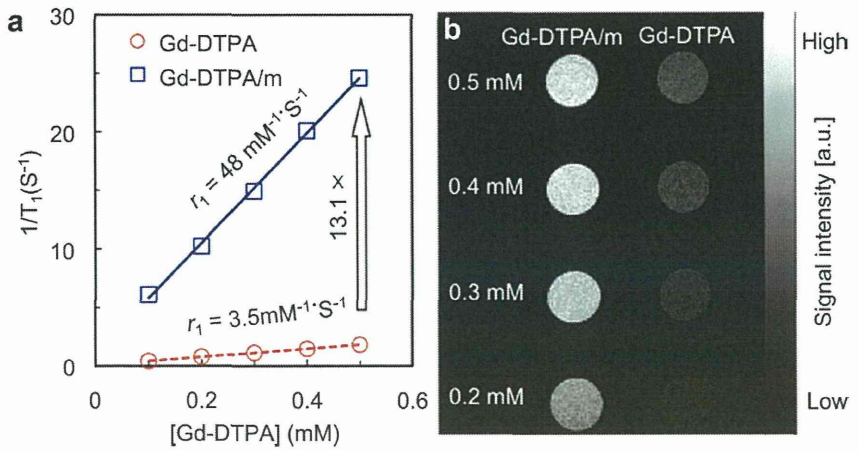

Fig. 4. MR enhancement effect of Gd-DTPA/m. (a) T_1 relaxivity coefficient. (b) T_1 weight MR images of Gd-DTPA/m and free Gd-DTPA solutions at 1 T.

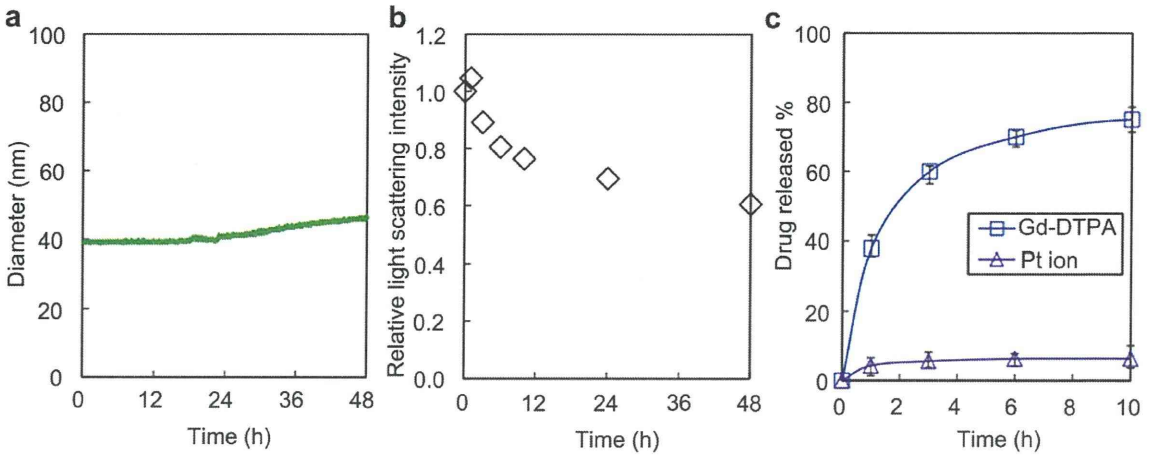

Fig. 5. Physicochemical characterization of Gd-DTPA/m under physiologic conditions. (a) Real time changes of diameter and (b) Change in relative light scattering intensity of Gd-DTPA/m. (c) Release rate of Gd-DTPA and Pt complexes from Gd-DTPA/m under similar conditions.

formation of micelles as without K_2PtCl_6, or even at low K_2PtCl_6 concentration, the micelles did not assemble (Fig. 1a and b). At 5 and 10 mM of K_2PtCl_6, narrowly distributed micelles were formed incorporating 16% and 12% of Gd-DTPA in weight, respectively (Table 1). Besides, the micelles prepared with PEG-*b*-Asp(DET) having longer PAsp(DET) segments showed higher loading of Gd-DTPA (DP = 45, 16%) than those PAsp(DET) with shorter segments (8% for DP = 25, and 9% for DP = 35) as shown in Table S1. Therefore, we decided to use Gd-DTPA/m prepared from PEG-*b*-PAsp(DET) (DP = 45), 5 mM Gd-DTPA and 5 mM K_2PtCl_6 for all of the following experiments as this composition produced micelles with highest Gd-DPTA loading. In addition, we confirmed that K_2PtCl_6 did not break the Gd-DTPA chelates as Gd^{3+} was not detectable, by arsenazo III method [31], at any ratio of Gd-DTPA/K_2PtCl_6 (Fig. 2).

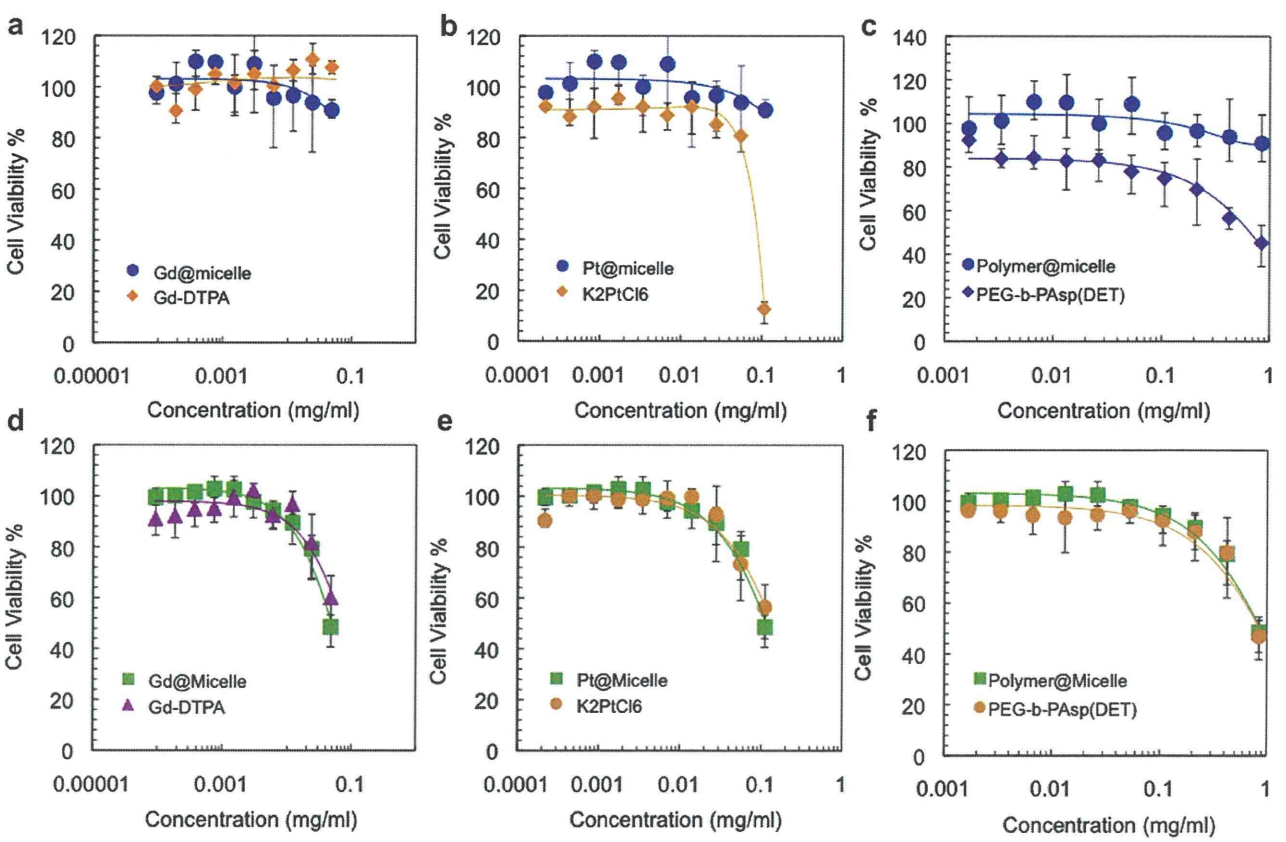

Fig. 6. Cytotoxicity of Gd-DTPA/m against HUVEC (a–c) and murine melanoma B16-F10 cells (d–f) after 72 h incubation. Micelles show comparable or even higher cell viability than free components, i.e., Gd-DTPA, K_2PtCl_6 and PEG-*b*-PAsp(DET).

The *z*-average diameter by intensity of these micelles was approximately 45 nm according to dynamic light scattering (Fig. 1c), and their zeta-potential was close to neutral at pH 7.4 (Figure S5). Diameter of sub-50 nm nanocarriers is important to achieve their deep tumor penetration in poorly permeable tumors according to our recent study [34]. Thus, the size of Gd-DTPA/m may be suitable for MR imaging of solid tumors with reduced permeability. According to TEM, Gd-DTPA/m showed quite narrowly distributed spherical morphology (Fig. 1d, e and Figure s6). Accordingly, the average size of the Gd-DTPA/m was calculated to be 22 nm (Fig. 1f), which is consistent with the number-averaged distribution (23 nm) calculated from *z*-averaged data obtained by DLS.

The elemental mapping under scanning TEM (STEM) and energy dispersive X-ray spectroscopy (EDS) of Gd-DTPA/m (Fig. 3) proved the existence of Gd and Pt elements inside the core of micelles. These results correlate with ICP-MS data (Table 1) as Pt concentration is higher than Gd encapsulated inside micelle.

The relaxivity of Gd-DTPA/m increased to 48 mM^{-1} s^{-1} based on Gd-DTPA, which is approximately 13-fold higher than that of free Gd-DTPA (Fig. 4a). T_1-weighted spin echo MRI at 1 T also revealed that Gd-DTPA/m highly improved MR contrast enhancement

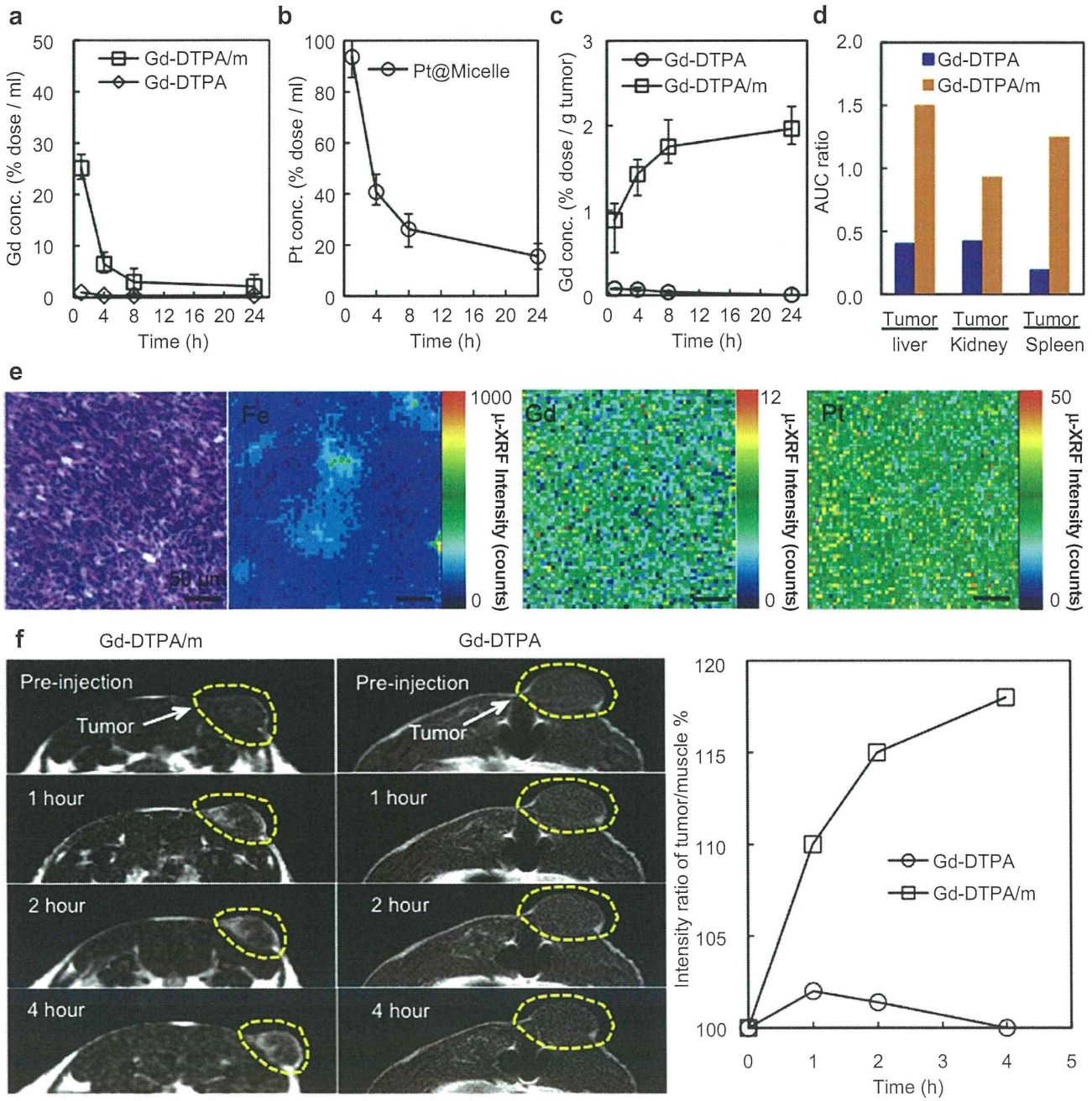

Fig. 7. *In vivo* evaluation of Gd-DTPA/m. (a) Plasma clearance of Gd-DTPA/m and free Gd-DTPA. (b) Plasma clearance of Pt@micelles. (c) Tumor accumulation of Gd-DTPA/m and free Gd-DTPA. (d) Tumor to tissue AUC ratios. (e) Microscopic findings (H&E staining) of tumor tissue and element distribution in tumor section. (f) T_1 weight tumor contrast enhancement after i.v. injection of Gd-DTPA loaded micelle and free Gd-DTPA.

compared to free Gd-DTPA (Fig. 3b), which may be attributed to a prolongation of the rotational correlation time, τ_R, due to restricted local motion similar to that of Gd-DTPA bound to macromolecules [35]. The benefits of slow rotation are observed at lower field strengths as the prevailing correlation time is almost always rotational diffusion, while at higher magnetic fields, the relaxivity of these Gd^{3+} complexes immobilized on slowly tumbling macromolecules rapidly decreases [36–38]. Accordingly, T_1-weighted spin echo MRI at 7 T showed that the contrast of Gd-DTPA/m was similar to free Gd-DTPA (Figure S7). Since clinical MRI machines use magnetic fields as high as 1.5 T, the design of Gd-DTPA/m is suitable for high relaxivity contrast enhancement at low dose. Interestingly, r_1 of Gd-DTPA/m augmented as the Pt/Gd ratio inside the core increased (Figure S8). Conversely, the r_1 relaxivity of Gd-DTPA/K_2PtCl_6 mixtures at different mole ratios or incubation time showed no significant r_1 relaxivity enhancement (Figure S9) suggesting that the incorporation of Gd-DTPA in the micelles core is necessary for the enhancement of relaxivity.

The micelles were stable under physiological conditions, i.e. in 10 mM PBS (pH 7.4) with 150 mM NaCl at 37 °C. In physiological environments, the diameter of the micelles slightly augmented after 18–20 h (Fig. 5a). Moreover, 60% of the initial light scattering intensity of the micelles was detectable even after 48 h (Fig. 5b). During the exposure of the micelles to physiological conditions, 75% Gd-DTPA was released in approximately 10 h, while only 7% of Pt was released probably due to stable metal complexation of Pt(IV) with PEG-*b*-PAsp(DET) (Fig. 5c). The ability of Gd-DTPA/m to sustainedly release Gd-DTPA, which can undergo glomerular filtration in the kidneys, may reduce the risk of free Gd discharge in the body.

Gd-DTPA/m was not cytotoxic against both primary cell lines (HUVEC) and tumor cell lines (B16-F10) (Fig. 6), suggesting its safety for *in vivo* application. Gd-DTPA/m extended the circulation of Gd-DTPA in the bloodstream, attaining 5% of the injected dose of Gd-DTPA after 8 h, while free Gd-DTPA was rapidly cleared from plasma (Fig. 7a and b). Moreover, approximately 15% of the injected Pt remained in the bloodstream after 24 h, which indicates the circulation of the micelles in the bloodstream. Gd-DTPA/m was able to deliver 26-fold higher CA in subcutaneous murine colon adenocarcinoma 26 (C-26) than free Gd-DTPA (Fig. 7c). In addition, the ratio of AUC in tumor versus organs indicated that Gd-DTPA/m improved the tumor-to-organ distribution of Gd-DTPA (Fig. 7d).

The microdistribution of the drugs at the tumor site was studied by micro-synchrotron radiation-induced X-ray fluorescence spectrometry imaging (μ-SR-XRF) of the tumor sites as Pt and Gd showed very distinct peaks in the sum spectrum of the line scan. Moreover, Fe mapping was also evaluated as it characterizes hemeproteins and therefore the positioning of blood vessels in the tissue. The atoms of Gd as well as Pt located in the whole tumor section in areas far from the Fe-rich regions suggesting deep tumor penetration and accumulation of Gd-DTPA/m as shown in Fig. 7e, in which the rainbow scales represent the quantity of element.

The size, neutral surface charge, stability and release characteristics of Gd-DTPA/m may contribute to the high penetration and accumulation of Gd-DTPA at the tumor site. The higher tumor accumulation and higher relaxivity of Gd-DTPA/m clearly and selectively enhanced the contrast at the tumor area in T_1-weighted MR images, even at low dose (0.02 mmol/kg based on Gd-DTPA) of contrast agents (Fig. 7f). The tumor selective contrast enhancement of Gd-DTPA/m was significant from 1 h after injection until the end of the experiment, that is, 4 h after injection. Oppositely, intravenously injected free Gd-DTPA, even at a 10 times higher dose, that is, 0.22 mmol/kg, failed to increase the intensity of the signal in the tumor region. These findings indicate the potential of GD-DTPA/m as a tumor-selective contrast agent.

4. Conclusion

Gd-DTPA/m efficiently improved the MRI-contrast of solid tumors demonstrating its potential application in the bio-imaging field. Accordingly, the sub-50 nm size, neutral surface and biological stability of Gd-DTPA/m, and the increased relaxivity of Gd-DTPA in the core of micelles lead to selective contrast enhancement of tumors. This facile and reversible metal complexation used for the construction of Gd-DTPA/m could also be applied for incorporating hydrophilic imaging probes, therapeutic drugs, or bioactive molecules into nanodevices for diagnosis and therapy. Accordingly, here, we illustrated a new approach for designing nano-sized vehicles by incorporating drugs via metal complexation besides widely used methods, such as covalent conjugation, or hydrophobic interaction, demonstrating its further application for loading compounds, which are difficult to incorporate in traditional nanocarriers.

Acknowledgments

This work was financially supported by the Japan Society for the Promotion of Science (JSPS) through its "Funding Program for World-Leading Innovative R&D on Science and Technology (FIRST Program)". TEM experiments were conducted in Research Hub for Advanced Nano Characterization, The University of Tokyo, supported by the Ministry of Education, Culture, Sports, Science and Technology (MEXT), Japan. P. M. acknowledges the fellowship from Ministry of Education, Science, Sports and Culture (MEXT), Japan. The authors are grateful Mr. Hashime Hoshi (JEOL), Ms. Sayaka Shibata and Aiko Sekita (NIRS) for technical support.

Appendix A. Supplementary data

Supplementary data related to this article can be found at http://dx.doi.org/10.1016/j.biomaterials.2012.09.030.

References

[1] Weissleder R, Pittet MJ. Imaging in the era of molecular oncology. Nature 2008;452:580–9.
[2] Mansfield P. Snapshot magnetic resonance imaging. Angew Chem Int Ed 2004; 43:5456–64.
[3] Weinmann HJ, Brasch RC, Press WR, Wesbey GE. Characteristics of gadolinium-DTPA complex: a potential NMR contrast agent. AJR Am J Roentgenol 1984; 142:619–24.
[4] Davis PL, Kaufman L, Crooks LE, Miller TR. Detectability of hepatomas in rat livers by nuclear magnetic resonance imaging. Invest Radiol 1981;16:354–9.
[5] Laurent S, Elst LV, Muller RN. Comparative study of the physicochemical properties of six clinical low molecular weight gadolinium contrast agents. Contrast Media Mol Imaging 2006;1:128–37.
[6] Ananta JS, Godin B, Sethi R, Moriggi L, Liu XW, Serda RE, et al. Geometrical confinement of gadolinium-based contrast agents in nanoporous particles enhances T-1 contrast. Nat Nanotech 2010;5:815–21.
[7] Thompson KH, Orvig C. Boon and bane of metal ions in medicine. Science 2003;300:936–9.
[8] Ferrari M. Cancer nanotechnology: opportunities and challenges. Nat Rev Cancer 2005;5:161–71.
[9] Cabral H, Nishiyama N, Kataoka K. Supramolecular nanodevices: from design validation to theranostic nanomedicine. Acc Chem Res 2011;44:999–1008.
[10] Kataoka K, Harada A, Nagasaki Y. Block copolymer micelles for drug delivery: design, characterization and biological significance. Adv Drug Deliv Rev 2001; 47:113–31.
[11] Nishiyama N, Morimoto Y, Jang WD, Kataoka K. Design and development of dendrimer photosensitizer-incorporated polymeric micelles for enhanced photodynamic therapy. Adv Drug Deliv Rev 2009;61:327–38.
[12] Rafi M, Cabral H, Kano MR, Mi P, Iwata C, Yashiro M, et al. Polymeric micelles incorporating (1,2-diaminocyclohexane)platinum (II) suppress the growth of orthotopic scirrhous gastric tumors and their lymph node metastasis. J Control Release 2012;159:189–96.
[13] Mikhaylov G, Mikac U, Magaeva AA, Itin VI, Naiden EP, Psakhye I, et al. Ferri-liposomes as an MRI-visible drug-delivery system for targeting tumours and their microenvironment. Nat Nanotech 2011;6:594–602.

[14] Floyd III WC, Klemm PJ, Smiles DE, Kohlgruber AC, Pierre VC, Mynar JL, et al. Conjugation effects of various linkers on Gd(III) MRI contrast agents with dendrimers: optimizing the hydroxypyridinonate (HOPO) ligands with nontoxic, degradable esteramide (EA) dendrimers for high relaxivity. J Am Chem Soc 2011;133:2390–3.
[15] Kojima C, Turkbey B, Ogawa M, Bernardo M, Regino CAS, Bryant LH, et al. Dendrimer-based MRI contrast agents: the effects of PEGylation on relaxivity and pharmacokinetics. Nanomedicine 2011;7:1001–8.
[16] Khemtong C, Kessinger CW, Ren J, Bey EA, Yang SG, Guthi JS, et al. In vivo off-resonance saturation magnetic resonance imaging of alphavbeta3-targeted superparamagnetic nanoparticles. Cancer Res 2009;69:1651–8.
[17] Mulder WJM, Strijkers GJ, van Tilborg GAF, Griffioen AW, Nicolay K. Lipid-based nanoparticles for contrast-enhanced MRI and molecular imaging. NMR Biomed 2006;19:142–64.
[18] Ai H. Layer-by-layer capsules for magnetic resonance imaging and drug delivery. Adv Drug Deliv Rev 2011;63:772–88.
[19] Vucic E, Sanders HM, Arena F, Terreno E, Aime S, Nicolay K, et al. Well-defined, multifunctional nanostructures of a paramagnetic lipid and a lipopeptide for macrophage imaging. J Am Chem Soc 2009;131:406–7.
[20] Kaida S, Cabral H, Kumagai M, Kishimura A, Terada Y, Sekino M, et al. Visible drug delivery by supramolecular nanocarriers directing to single-platformed diagnosis and therapy of pancreatic tumor model. Cancer Res 2010;70:7031–41.
[21] Nasongkla N, Bey E, Ren JM, Ai H, Khemtong C, Guthi JS, et al. Multifunctional polymeric micelles as cancer-targeted, MRI-ultrasensitive drug delivery systems. Nano Lett 2006;6:2427–30.
[22] Yokoyama M, Nakamura E, Makino K, Okano T, Yamamoto TA. Polymeric micelle MRI contrast agent with changeable relaxivity. J Control Release 2006; 114:325–33.
[23] Manus LM, Mastarone DJ, Waters EA, Zhang XQ, Schultz-Sikma EA, MacRenaris KW, et al. Gd(III)-nanodiamond conjugates for MRI contrast enhancement. Nano Lett 2010;10:484–9.
[24] Torchilin VP. PEG-based micelles as carriers of contrast agents for different imaging modalities. Adv Drug Deliv Rev 2002;54:235–52.
[25] Ai H, Flask C, Weinberg B, Shuai X, Pagel MD, Farrell D, et al. Magnetite-loaded polymeric micelles as ultrasensitive magnetic-resonance probes. Adv Mater 2005;17:1949–52.
[26] Duncan R, Izzo L. Dendrimer biocompatibility and toxicity. Adv Drug Deliv Rev 2005;57:2215–37.
[27] Matsumura Y, Kataoka K. Preclinical and clinical studies of anticancer agent-incorporating polymer micelles. Cancer Sci 2009;100:572–9.
[28] Plummer R, Wilson RH, Calvert H, Boddy AV, Griffin M, Sludden J, et al. A phase I clinical study of cisplatin-incorporated polymeric micelles (NC-6004) in patients with solid tumours. Br J Cancer 2011;104:593–8.
[29] Harada A, Kataoka K. Formation of polyion complex micelles in an aqueous milieu from a pair of oppositely-charged block-copolymers with poly(ethylene glycol) segments. Macromolecules 1995;28:5294–9.
[30] Kanayama N, Fukushima S, Nishiyama N, Itaka K, Jang WD, Miyata K, et al. A PEG-based biocompatible block catiomer with high buffering capacity for the construction of polyplex micelles showing efficient gene transfer toward primary cells. ChemMedChem 2006;1:439–44.
[31] Gouin S, Winnik FM. Quantitative assays of the amount of diethylene-triaminepentaacetic acid conjugated to water-soluble polymers using isothermal titration calorimetry and colorimetry. Bioconjug Chem 2001;12: 372–7.
[32] Itaka K, Ishii T, Hasegawa Y, Kataoka K. Biodegradable polyamino acid-based polycations as safe and effective gene carrier minimizing cumulative toxicity. Biomaterials 2010;31:3707–14.
[33] Iakovidis A, Hadjiliadis N. Complex-compounds of platinum(II) and platinum(IV) with amino-acids, peptides and their derivatives. Coord Chem Rev 1994;135:17–63.
[34] Cabral H, Matsumoto Y, Mizuno K, Chen Q, Murakami M, Kimura M, et al. Accumulation of sub-100nm polymeric micelles in poorly permeable tumours depends on size. Nat Nanotech 2011;6:815–23.
[35] Caravan P, Ellison JJ, McMurry TJ, Lauffer RB. Gadolinium(III) chelates as MRI contrast agents: structure, dynamics, and applications. Chem Rev 1999;99: 2293–352.
[36] Terreno E, Castelli DD, Viale A, Aime S. Challenges for molecular magnetic resonance imaging. Chem Rev 2010;110:3019–42.
[37] Mastarone DJ, Harrison VSR, Eckermann AL, Parigi G, Luchinat C, Meade TJ. A modular system for the synthesis of multiplexed magnetic resonance probes. J Am Chem Soc 2011;133:5329–37.
[38] Caravan P, Farrar CT, Frullano L, Uppal R. Influence of molecular parameters and increasing magnetic field strength on relaxivity of gadolinium- and manganese-based T1 contrast agents. Contrast Media Mol Imaging 2009;4: 89–100.

Journal of Controlled Release 161 (2012) 868–874

Contents lists available at SciVerse ScienceDirect

Journal of Controlled Release

journal homepage: www.elsevier.com/locate/jconrel

Pancreatic cancer therapy by systemic administration of VEGF siRNA contained in calcium phosphate/charge-conversional polymer hybrid nanoparticles

Frederico Pittella [a,b], Kanjiro Miyata [a], Yoshinori Maeda [b], Tomoya Suma [b], Sumiyo Watanabe [a], Qixian Chen [c], R. James Christie [a], Kensuke Osada [c], Nobuhiro Nishiyama [a], Kazunori Kataoka [a,b,c,d,*]

[a] Division of Clinical Biotechnology, Center for Disease Biology and Integrative Medicine, Graduate School of Medicine, The University of Tokyo, 7-3-1 Hongo, Bunkyo-ku, Tokyo 113-0033, Japan
[b] Department of Bioengineering, Graduate School of Engineering, The University of Tokyo, 7-3-1 Hongo, Bunkyo-ku, Tokyo 113-8656, Japan
[c] Department of Materials Engineering, Graduate School of Engineering, The University of Tokyo, 7-3-1 Hongo, Bunkyo-ku, Tokyo 113-8656, Japan
[d] Center for NanoBio Integration, The University of Tokyo, 7-3-1 Hongo, Bunkyo-ku, Tokyo 113-8656, Japan

ARTICLE INFO

Article history:
Received 16 February 2012
Accepted 1 May 2012
Available online 11 May 2012

Keywords:
siRNA
Calcium phosphate
Nanoparticle
VEGF
PEG
Charge-conversional polymer

ABSTRACT

Development of an efficient *in vivo* delivery vehicle of small interfering RNA (siRNA) is the key challenge for successful siRNA-based therapies. In this study, toward systemic delivery of siRNA to solid tumors, a smart polymer/calcium phosphate (CaP)/siRNA hybrid nanoparticle was prepared to feature biocompatibility, reversible stability and endosomal escape functionality using a pH sensitive block copolymer of poly(ethylene glycol) and charge-conversional polymer (PEG-CCP), of which anionic functional groups could be converted to cationic groups in an endosomal acidic condition for facilitated endosomal escape. Nanoparticles were confirmed to be approximately 100 nm in size, narrowly dispersed and spherical. Also, the nanoparticle was highly tolerable in medium containing serum, while releasing the entrapped siRNA in a cytoplasm-mimicking ionic condition, presumably based on the equilibrium between CaP complexes and calcium ions. Further, the nanoparticle showed high gene silencing efficiency in cultured pancreatic cancer cells (BxPC3) without associated cytotoxicity. Ultimately, systemic administration of the nanoparticles carrying vascular endothelium growth factor (VEGF) siRNA led to the significant reduction in the subcutaneous BxPC3 tumor growth, well consistent with the enhanced accumulation of siRNA and the significant VEGF gene silencing (~68%) in the tumor. Thus, the hybrid nanoparticle was demonstrated to be a promising formulation toward siRNA-based cancer therapies.

1. Introduction

Since elucidation of the molecular pathway of ribonucleic acid interference (RNAi) [1], small interfering ribonucleic acid (siRNA) has emerged as a potential therapeutic agent for modulating the production of proteins associated with disease [2,3]. Several clinical trials employing siRNA-based cancer therapies are currently ongoing [3,4]. In many cases, siRNA has been applied with a delivery vehicle to facilitate accumulation within the therapeutic site of activity (cell cytoplasm). Incorporation of siRNA within delivery vehicles is performed to overcome barriers associated with transport of this fragile and highly anionic macromolecule, such as premature degradation by RNases and inefficient cellular internalization. Therefore, development of more effective delivery vehicles is currently a major challenge for improving siRNA therapies.

Calcium phosphate (CaP)-based nanoparticles are a promising siRNA delivery platform because of the fact that CaP is naturally generated in the body (thus well tolerated), and also encapsulates negatively charged molecules during precipitation [5,6]. In this regard, a strategy to control the growth of CaP/siRNA precipitates is essential for their utilization toward systemic delivery applications. Several previous studies, including ours, have developed successful strategies to control nanoparticle size on the order of several tens to one hundred nanometer by coating with poly(ethylene glycol) (PEG)-*b*-polyanions [7–10], PEG-functionalized bisphosphonate [11], lipid bilayer membranes [12], or even nucleic acids [13]. Notably, a PEG shell on the nanoparticle surface has the desirable functionality to reduce non-specific interactions with biomacromolecules in the bloodstream, termed stealth property, for improved pharmacokinetics as well as facilitated accumulation in solid tumors through enhanced permeability and retention (EPR) effect [14–17].

Once internalized by cells via endocytosis, nanoparticles are transported to endosomal compartments ultimately lysosome where they remain until degraded. To overcome the endosomal/lysosomal entrapment of CaP nanoparticles, we developed CaP/polymer hybrid

* Corresponding author at: Division of Clinical Biotechnology, Center for Disease Biology and Integrative Medicine, Graduate School of Medicine, The University of Tokyo, 7-3-1 Hongo, Bunkyo-ku, Tokyo 113-0033, Japan.
E-mail address: kataoka@bmw.t.u-tokyo.ac.jp (K. Kataoka).

0168-3659/$ – see front matter © 2012 Elsevier B.V. All rights reserved.
doi:10.1016/j.jconrel.2012.05.005

nanoparticles containing functionality designed to promote escape from these subcellular compartments. This was achieved using a block copolymer of PEG and an endosome-disrupting polyanion, poly(*N*″-{*N*′-[(*N*-*cis*-aconityl)-2-aminoethyl]-2-aminoethyl}aspartamide) (PAsp(DET-Aco)) [18]. PAsp(DET-Aco) is relatively stable at the extracellular pH of 7.4 but degrades at pH ~5.5 (lysosome pH) by cleavage of *cis*-aconitic amide linkages, thus reverting back to the parent polycation, PAsp(DET). This degradation event results in conversion of the polymer charge from anionic to cationic, and is thus termed a charge-conversional polymer (CCP) (Fig. 1) [19]. PAsp(DET) has been shown to exhibit a distinctive change in the structure of side chains between pH 7.4 and pH 5.5 due to protonation of amino groups, i.e., monoprotonated diaminoethane at pH 7.4 and diprotonated diaminoethane at pH 5.5, allowing pH-selective membrane disruption for efficient endosomal escape of nucleic acids without associated toxicity [20–25]. In addition, PEG-PAsp(DET-Aco) was confirmed to facilitate excellent colloidal dispersion of CaP nanoparticles, while also improving the endosomal escape of siRNA, resulting in efficient gene silencing to cultured pancreatic carcinoma cells (PanC-1) [18].

The present work reports the *in vivo* application of the CaP/block copolymer/siRNA hybrid nanoparticles prepared with PEG-PAsp(DET-Aco) for treatment of subcutaneous pancreatic tumor (BxPC3) models in mice by systemic administration. Removal of free calcium ions from CaP nanoparticle solutions is critical for its systemic administration, as excess calcium ions may induce adverse effects in the bloodstream [32]. Thus nanoparticle solutions were purified by ultrafiltration, and then characterized with non-purified controls in terms of stability, morphology, calcium amount and biological activity. For treatment of subcutaneous pancreatic tumors, the key pro-angiogenic molecule vascular endothelial growth factor (VEGF) was selected as the target gene, once it is known to be over-expressed in many cancerous cells, promoting angiogenesis through endothelial proliferation, survival and migration [26]. Moreover, silencing of the VEGF signaling pathway has been shown to suppress tumor angiogenesis and growth [27–30]. After systemic administration of purified nanoparticles incorporating VEGF siRNA for anti-angiogenic therapy, the accumulation of siRNA and the expression level of VEGF mRNA in the tumor tissue were evaluated to elucidate their correlation with tumor growth rates. This work demonstrates significant antitumor activity induced by VEGF gene silencing with siRNA delivered by CaP/block copolymer hybrid nanoparticles.

2. Materials and methods

2.1. Materials, cell line and animals

Dulbecco's modified eagle's medium (DMEM) without L-glutamine and phenol red, RPMI 1640 and *cis*-aconitic anhydride were purchased from Sigma-Aldrich (St. Louis, MO). α-Methoxy-ω-amino poly(ethylene glycol) (MeO–PEG–NH_2) (M_w: 12,000) and β-benzyl-L-aspartate *N*-carboxy anhydride (BLA-NCA) were obtained from NOF Co., Inc. (Tokyo, Japan) and Chuo Kaseihin Co., Inc. (Tokyo, Japan), respectively. *N*-methyl-2-pyrrolidone (NMP), diethylenetriamine (DET), dimethyl sulfoxide (DMSO), *N*,*N*-dimethylformamide (DMF), dichloromethane (DCM) and acetic anhydride were purchased from Tokyo Chemical Industry Co. Ltd. (Tokyo, Japan) or Nacalai Tesque (Tokyo, Japan), and used after conventional distillation. Acetic acid, acetonitrile, acetone, diethyl ether and hydrochloric acid were purchased from Wako Pure Chemical Industries Ltd. (Osaka, Japan). Fetal bovine serum (FBS) was purchased from Dainippon Sumitomo Pharma Co., Ltd. (Osaka, Japan). RT-PCR primers used for human actin and human VEGF were synthesized by Hokkaido System Science (Hokkaido, Japan) and the sequences are the following: CCAACCGCGAGAAGATGA (actin forward); CCAGAGGCGTACAGGGATAG (actin reverse); AGTGGTCCCAGGCTGCAC (VEGF forward); TCCATGAACTTCACCACTTCGT (VEGF reverse). All the siRNAs were synthesized by Hokkaido System Science (Hokkaido, Japan). The sequences of VEGF siRNA (siVEGF) are 5′-GGAGUACCCUGAUGAGAUCdTdT-3′ (sense) and 5′-GAUCUCAUCAGGGUACUCCdTdT-3′ (antisense), and the sequences of scramble siRNA (siSCR) are 5′-UUCUCCGAACGUGUCACGUdTdT-3′ (sense); 5′-ACGUGACACGUUCGGAGAAdTdT-3′ (antisense).

BxPC3 cells (human tumorigenic pancreatic adenocarcinoma, ATCC number: CRL-1687) were obtained from the American Type Culture Collection (Manassas, VA). Cells were maintained in RPMI 1640 medium (Sigma Chemical Co., Inc.) containing 10% fetal bovine serum (FBS) in a humidified atmosphere containing 5% CO_2 at 37 °C. Balb-c nu/nu mice (female; 18–20 g body weight; age, 6 weeks) were purchased from Charles River Japan (Kanagawa, Japan). All animal experiments were performed in accordance with the Guidelines for the Care and Use of Laboratory Animals as stated by the University of Tokyo.

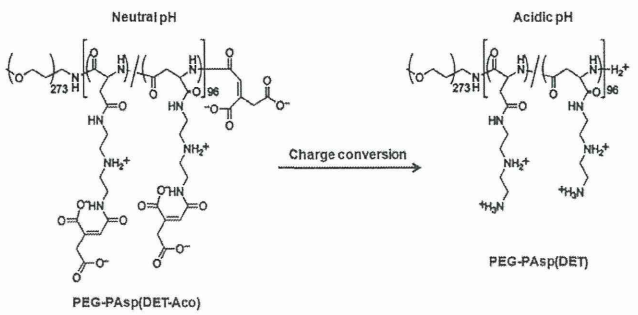

Fig. 1. Change in the chemical structure of PEG-PAsp(DET-Aco) to PEG-PAsp(DET) in response to the acidic pH.

2.2. Polymer synthesis

Detailed synthesis methods of the parent polycation PEG-PAsp(DET) and PEG-PAsp(DET-Aco) derivative are described in Supplementary data.

2.3. Preparation of PEG-CCP/siRNA/CaP hybrid nanoparticles

A solution of 2.5 M $CaCl_2$ (1 μL) was diluted in 10 mM Tris buffer (pH 10) (11.5 μL). Another solution containing PEG-PAsp(DET-Aco) (1.0 mg/mL) in 10 mM Tris/HCl buffer (pH 7.5) was mixed with a solution of 15 μM siRNA in 10 mM HEPES buffer (pH 7.2) and with 50 mM HEPES buffer containing 1.5 mM Na_3PO_4 and 140 mM NaCl (pH 7.5) (2.5 μL: 5 μL: 5 μL). The former solution was mixed with the latter solution by pipetting for around 20 s (final siRNA concentration; 3 μM).

2.4. Purification of PEG-CCP/siRNA/CaP hybrid nanoparticles

The purification of hybrid nanoparticles for removal of excess amount of free calcium ions was carried out immediately after preparation. PEG-CCP/siRNA/CaP hybrid nanoparticle solution containing 41.3 μg siRNA and 150 μg PEG-CCP (1 mL) was added to a VivaSpin-06 device (MWCO: 10 kDa) containing 1 mL of an extracellular (EC) buffer that mimics the ionic strength of extracellular environment (2 mM $CaCl_2$, 1 mM Na_2HPO_4, 25 mM Tris and 140 mM NaCl at pH 7.4) [8]. The mixture was centrifuged in a swing bucket rotor at 900 g and 4 °C for 20 min. To minimize non-specific binding of nanoparticles to the membrane, the centrifuge filter devices were washed with de-ionized water before use. After centrifugation, the retained solution was collected and used in further experiments.

2.5. Determination of calcium content in nanoparticles

The total calcium content present in the solution of non-purified and purified/concentrated hybrid nanoparticles was determined by the SRL Laboratories (SRL Inc., Tokyo, Japan) through spectrophotometry using

arsenazo III. All the samples were diluted four times with distilled water to the final volume of 300 μL before assay. The reaction of arsenazo III dye with calcium under acidic conditions produces a blue–purple complex, of which concentration is determined spectrophotometrically at the wavelength of 660 nm. Obtained values were used to calculate the efficiency of calcium removal from nanoparticle solution.

2.6. Dynamic light scattering (DLS) measurements

DLS measurements were carried out at 25 °C using a Zetasizer Nano ZS (Malvern Instruments, UK) at a detection angle of 173° with a He–Ne laser (633 nm) as the incident beam. The data obtained from the rate of decay in the photon correlation function were analyzed with a cumulant method to obtain the corresponding hydrodynamic diameters and polydispersity indices (PdI) (μ/G^2) of the nanoparticles. The colloidal stability of both purified and non-purified nanoparticles was monitored during several days and the result was presented as a relative size to the initial hydrodynamic diameter obtained in the first day.

2.7. Atomic force microscopy (AFM) imaging

AFM imaging of the nanoparticles was performed using a MMAFM, Nanoscope V (Bruker AXS, Madison, WI) in ScanAsyst Atomic Force Microscopy Imaging mode with standard silicon probes. Imaging was conducted under air on a highly orientated pyrolytic graphite (HOPG) substrate. The obtained images were processed by flattening to remove the background slope of the substrate surface.

2.8. Fluorescence correlation spectroscopy (FCS) measurements

FCS measurements were performed using a Confocor3 module (Carl Zeiss, Jena, Germany) equipped with a Zeiss C-Apochromat 40× water objective. Samples prepared with Cy5-labeled siRNA were measured with the excitation of a He–Ne laser (633 nm, 5 mW) and the emission passed through a 650 nm long pass filter. Samples were placed into 8-well Lab-Tek chambered borosilicate cover-glass slides (Nalge Nunc International, Rochester, NY). Determination of the focal volume was established by calibration with 10 nM Cy5 standard solution. Each analysis consisted of 10 measurements with a sampling time of 20 s and the measured autocorrelation curves were fitted with the Zeiss Confocor3 software package to obtain the diffusion coefficient. The stability of nanoparticles under a cell culture condition was evaluated after dilution of samples with DMEM containing 10% FBS without L-glutamine and phenol red and then incubation at 37 °C. The stability of nanoparticles in the solution mimicking the intracellular fluids was evaluated after dilution of the samples with the ionic solution ($CaCl_2$ 100 nM, Na_2HPO_4 40 mM, NaCl 140 mM, pH 7.4), as previously described [8]. The concentration of Cy5-labeled siRNA was adjusted to 100 nM, corresponding to the *in vitro* gene silencing experiment.

2.9. In vitro gene silencing

To evaluate the gene silencing efficiency of the purified nanoparticles compared to non-purified controls, BxPC3 cells were seeded with 2 mL of RPMI 1640 containing 10% FBS on a 6 well plate at 5×10^4 cells/well. After 24 h, nanoparticle solutions were added with fresh medium (100 nM siRNA). After another 24 h, cells were harvested and RNA was extracted using RNeasy Mini Kit (Qiagen, Valencia, CA), according to the manufacturer's instruction.

2.10. Real-time reverse transcriptional (RT)-PCR

After obtaining the RNA from cells or tissue, the RNA concentration was measured and then sample concentrations were normalized. Next, the genomic DNA elimination was performed prior to cDNA synthesis using a QuantiTect Reverse Transcription kit (Qiagen, Valencia, CA). Real-time RT-PCR was performed using an ABI 7500 Fast Real-time RT-PCR System (Applied Biosystems, Foster City, CA) and QuantiTect SYBR Green PCR Master Mix (Qiagen, Valencia, CA). Actin was used as the house-keeper gene and the obtained data were normalized before statistical analysis.

2.11. Antitumor activity

Balb/c nude mice (female, 6 week old) were subcutaneously implanted with BxPC3 tumor (3 mm×3 mm×1 mm). The tumors were allowed to grow for 3 weeks before sample injection. Further, the mice bearing tumors with similar volume (~50 mm^3) were randomly distributed in groups ($n=4$). Thereafter, hybrid nanoparticles loading siVEGF (25 μg siRNA in 200 μL per injection) were injected into the tail vein 4 times at days 2, 5, 8 and 12. Tumor size and body weight for each mouse were monitored for 13 days. The tumor volume was calculated based on a modified ellipsoidal formula [30,31]: tumor volume = $1/2(\text{length}\times\text{width}^2)$.

2.12. Tumor accumulation

Similarly to Section 2.11, BxPC3 tumor-bearing mice were prepared by subcutaneous implantation of the tumor pieces (3 mm×3 mm×1 mm). The tumors were allowed to grow for 4 weeks before sample injection. Five mice bearing tumors of the similar volume (~70 mm^3) were randomly selected for each cohort ($n=5$). Hybrid nanoparticles containing Cy5-labeled siRNA were intravenously injected into the tail vein at 15 μg of Cy5-labeled siRNA per injection. Mice were sacrificed 60 min after injection and tumors were excised. Cy5 fluorescence from the tumor tissue was measured by IVIS (Caliper Life Sciences, Hopkinton, MA). Results were expressed as total photon counts normalized by tumor weight.

2.13. In vivo gene silencing in tumor tissue

BxPC3 tumor-bearing mice were prepared by subcutaneous implantation of the tumor pieces (3 mm×3 mm×1 mm) and then allowed to grow for 4 weeks, similar to the method described in Sections 2.11 and 2.12. Mice bearing tumors of similar volume (~70 mm^3) were randomly distributed in groups ($n=3$). Thereafter, hybrid nanoparticles loading siVEGF (25 μg siRNA in 200 μL per injection) were injected into the tail vein on days 1, 4, 8 and 34. After 24 h of the last injection, each tumor was excised and the non-necrotic part of the tumor (~20 mg) was cut into small pieces and sonicated for 10 s in a lysis buffer. The lysate was centrifuged and then the supernatant was used to extract RNA using the RNeasy Mini Kit (Qiagen, Valencia, CA), according to the manufacturer's instruction. Extracted RNA was further used to verify VEGF gene silencing by real-time RT-PCR, as described in Section 2.10.

3. Results and discussion

3.1. Preparation and purification/concentration of hybrid nanoparticles

The functional CCP block copolymer, PEG-PAsp(DET-Aco) (Fig. 1), was synthesized using a procedure similar to our previous report [18]. Successful synthesis of PEG-PAsp(DET-Aco) was confirmed from the ^{1}H NMR spectrum (Supporting Fig. 1) by the appearance of protons present on acid-labile *cis*-aconitic amide (Aco) moieties. This introduction is accompanied by the conversion of cationic charges to negative charges in the polyaspartamide side chain, enabling integration of PEG-CCP into CaP nanoparticles. The prepared charge-conversional polymer shows high stability at neutral pH but becomes cleavable at acidic pH to reproduce cationic PAsp(DET) from anionic PAsp(DET-Aco) (Fig. 1). Note that, once in the acidic environment of the endosome/lysosome, PAsp(DET) can disrupt their membrane to facilitate the escape of nanoparticles from these compartments [18,25].